VOL. 20, NO. 9, SEPTEMBER 1982 AIAA JOURNAL 1219

AIAA 81-1474R

Navier-Stokes Solutions for an Axisymmetric Nozzle

G. A. Hasen[*]
Air Force Wright Aeronautical Laboratories, Wright-Patterson Air Force Base, Ohio

Numerical solutions of the Navier-Stokes equations are obtained for an axisymmetric nozzle in a supersonic external flowfield ($M_\infty = 1.94$, $M_j = 3.0$, $Re_\infty = 2.2 \times 10^6$). Five jet pressure ratio conditions ranging from a highly overexpanded case that exhibits a Mach disk shock formation to a slightly underexpanded case are solved computationally. MacCormack's explicit finite-difference algorithm, an adaptive grid scheme, and locally dependent eddy viscosity modeling are utilized to obtain the numerical solutions. The computational results accurately reproduce the experimentally observed viscous effects on the nozzle base pressure and shock locations resulting from a thick base annulus on the nozzle. Correct transition from regular shock reflection to Mach disk reflection in the jet core was achieved numerically.

Nomenclature

C_p = specific heat at constant pressure
C_v = specific heat at constant volume
e = specific energy, $C_v T + (u^2 + v^2)/2$
F,G = flux vectors
f = primitive flow variable, ρ, u, v, or T
H = axisymmetric flux vector
j_0 = exponent parameter equal to 0 or 1 for two-dimensional or axisymmetric flow, respectively
k = thermal conductivity
L = length scale
L_ξ, L_η = MacCormack difference operators in the ξ and η directions
M = Mach number
P = static pressure
Pr = Prandtl number
P_{T2} = pitot pressure
$\mathcal{P}_B$ = base pressure coefficient, $(P_b - P_\infty)/q_\infty$
q = dynamic pressure, $\gamma PM^2/2$
$\dot{q}_x, \dot{q}_r$ = heat flux in the axial and radial directions
R = gas constant for air
Re = Reynolds number based on body length
T = static temperature
t = time
U = conservative flow variable vector
u,v = velocity components in the axial and radial directions
V = velocity vector
x,r = Cartesian coordinates
γ = ratio of specific heats, C_p/C_v
δ = mixing layer thickness
ϵ = turbulent eddy viscosity coefficient
ξ,η = normalized Cartesian coordinates in the computational plane
λ = viscosity diffusion coefficient
μ = molecular viscosity coefficient
ρ = density
σ = normal stress
τ_{xr} = shear stress
ω = vorticity

Superscript

n = evaluated at time $n\Delta t$

Subscripts

e = evaluated at boundary-layer edge
i,j = grid point indices
j = evaluated in the jet flow
t = turbulent flow
∞ = evaluated in the freestream

Introduction

THE increased importance of aft-end drag associated with nozzle installations in current and future high-performance aircraft has led to extensive and very costly experimental nozzle test programs. Computational aerodynamics shows great promise as a field that can have a favorable impact on this requirement for nozzle testing. Boundary-layer and shear layer growth, separation, shock formation and reflection, and plume blockage and entrainment characteristic of nozzle flows can be analyzed using computational techniques. Unlike experimental testing, computational analysis is not necessarily restricted by Reynolds number or nozzle exhaust temperature limitations, and the effects of support stings and test section walls on the flowfield of interest can be eliminated. Since the cost of computational analysis is decreasing as more advanced computers are developed, while experimental costs are steadily increasing, computational analysis is being investigated in much more detail.

Early computational viscous solutions of the aft-end or nozzle flowfield region[1-4] consisted of patching methods that divided the flowfield into an inviscid freestream, an inviscid jet stream, and a viscous boundary layer and mixing layer. Each of these regions was analyzed independently and was iteratively coupled using appropriate boundary conditions. Although these solutions gave reasonable results for specific data sets, the required empirical matching limited the usefulness of this method as a predictive technique. Later solutions involved solving the time-dependent, compressible Navier-Stokes equations uniformly over the entire nozzle flowfield. Solutions of this type involve both plume simulators[5,6] and actual jet exhaust flows.[7,8] In this more adaptive, direct approach, the predominantly inviscid and viscous regions are solved simultaneously, with no matching required.

Navier-Stokes solutions are especially useful for predicting off-design nozzle characteristics where the flowfield is in either a significantly overexpanded or an underexpanded state. At these conditions the structure of the flow is more complex, with viscous regions becoming more prevalent. Two features typical of these off-design conditions are the establishment of a triple point in the flow and the appearance of a strong normal shock referred to as a Mach disk (see Fig.

Presented as Paper 81-1474 at the AIAA/SAE/ASME 17th Joint Propulsion Conference, Colorado Springs, Colo., July 27-29, 1981; submitted Aug. 12, 1981; revision received Jan. 8, 1982. This paper is declared a work of the U.S. Government and therefore is in the public domain.

[*] Captain, USAF; Computational Aerodynamics Engineer. Member AIAA.

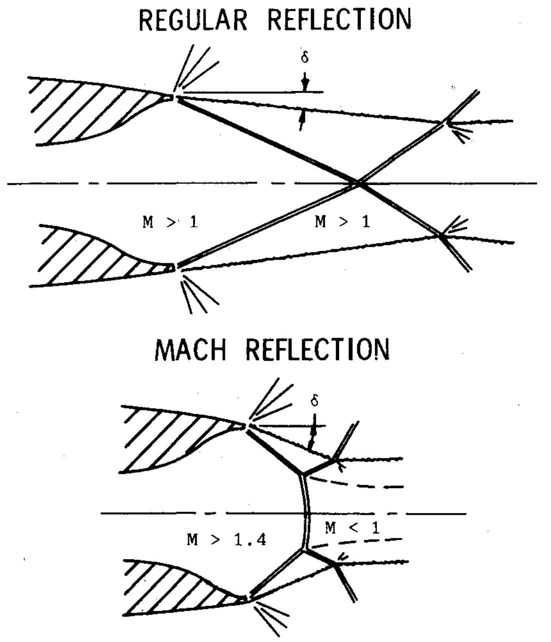

Fig. 1 Shock structure for a typical overexpanded axisymmetric nozzle.

1). This phenomenon has not been simulated adequately in the past using numerical techniques. Several empirical techniques have been developed,[9-11] but none applies to a wide range of pressure ratios. Inviscid analyses using a combination of the method of characteristics and the method of integral relations[12,13] or inviscid time-dependent solutions[14,15] have been performed, but these analyses are limited by viscous effects that tend to influence the flow patterns and shock structure.

A full Navier-Stokes solution that includes viscous effects present at these off-design conditions is necessary to simulate this type of flow adequately. The purpose of this investigation was to develop a numerical Navier-Stokes method capable of accurately predicting supersonic nozzle flowfields that contain both highly viscous flow regions and complex shock structure typified by the Mach disk formation. Overexpanded nozzle flowfields were simulated numerically, since they met the previous conditions while possessing fairly compact flow domains. Solutions for an axisymmetric convergent-divergent nozzle with a thick base annulus in a supersonic external flowfield were obtained for five pressure ratios ranging from a slightly underexpanded condition to a highly overexpanded condition that exhibits the Mach disk structure.

Method of Solution

Governing Equations

The governing equations for a compressible, viscous fluid in the absence of body forces consist of the unsteady Navier-Stokes equations. These equations can be written in conservative form as follows:

$$\frac{\partial U}{\partial t} + \frac{\partial F}{\partial x} + \frac{1}{r^{j_0}} \frac{\partial}{\partial r} (r^{j_0} G) = j_0 \frac{H}{r^{j_0}} \tag{1}$$

where $j_0 = 0$ or 1 for either two-dimensional or axisymmetric flow, respectively, and

$$U = \begin{bmatrix} \rho \\ \rho u \\ \rho v \\ \rho e \end{bmatrix} \qquad F = \begin{bmatrix} \rho u \\ \rho u^2 - \sigma_{xx} \\ \rho u v - \tau_{xr} \\ \rho u e + \dot{q}_x - u\sigma_{xx} - v\tau_{xr} \end{bmatrix}$$

$$G = \begin{bmatrix} \rho v \\ \rho u v - \tau_{xr} \\ \rho v^2 - \sigma_{rr} \\ \rho v e + \dot{q}_r - u\tau_{xr} - v\sigma_{rr} \end{bmatrix} \qquad H = \begin{bmatrix} 0 \\ 0 \\ -\sigma_H \\ 0 \end{bmatrix}$$

The stress and heat-transfer components are given as:

$$\sigma_{xx} = -P + (\lambda + \lambda_t) \nabla \cdot V + 2(\mu + \epsilon) \frac{\partial u}{\partial x} \tag{2}$$

$$\sigma_{rr} = -P + (\lambda + \lambda_t) \nabla \cdot V + 2(\mu + \epsilon) \frac{\partial v}{\partial r} \tag{3}$$

$$\sigma_H = -P + (\lambda + \lambda_t) \nabla \cdot V + 2(\mu + \epsilon) \frac{v}{r} \tag{4}$$

$$\tau_{xr} = (\mu + \epsilon) \left(\frac{\partial u}{\partial r} + \frac{\partial v}{\partial x} \right) \tag{5}$$

$$\dot{q}_x = -C_p \left(\frac{\mu}{Pr} + \frac{\epsilon}{Pr_t} \right) \frac{\partial T}{\partial x} \tag{6}$$

$$\dot{q}_r = -C_p \left(\frac{\mu}{Pr} + \frac{\epsilon}{Pr_t} \right) \frac{\partial T}{\partial r} \tag{7}$$

The fluid (air) is assumed to obey the perfect-gas law, the coefficient of viscosity is assumed to vary according to Sutherland's formula, and the second coefficient of viscosity is assumed to follow Stokes' hypothesis:

$$(\lambda + \lambda_t) = -\tfrac{2}{3} (\mu + \epsilon) \tag{8}$$

Other relationships needed to complete the system of equations include the definition of an eddy viscosity model and the specification of the molecular Prandtl number (0.72) and the turbulent Prandtl number (0.90).

For numerical computation in a transformed (ξ, η) Cartesian plane, the matrix form of the Navier-Stokes equations can be written as

$$\frac{\partial U}{\partial t} + \left[\xi_x \frac{\partial F}{\partial \xi} + \frac{1}{r^{j_0}} \xi_r \frac{\partial (r^{j_0} G)}{\partial \xi} \right] + \left[\eta_x \frac{\partial F}{\partial \eta} + \frac{1}{r^{j_0}} \eta_r \frac{\partial (r^{j_0} G)}{\partial \eta} \right] = j_0 \frac{H}{r^{j_0}} \tag{9}$$

where ξ and η are now the independent variables, and the transformation derivatives ξ_x, ξ_r, η_x, and η_r are obtained numerically using a mapping procedure.

Boundary Conditions

Since the solution of the Navier-Stokes equations is a mixed initial-boundary value problem, both initial conditions and boundary conditions must be specified for a given computational domain. The domain of interest for a symmetric nozzle is shown in Fig. 2. The following boundary and initial conditions are then specified for this domain (Fig. 3).

Upstream Boundaries

Inflow conditions at the upstream boundaries are completely specified and held fixed during the solution procedure. A relatively coarse grid, parabolized Navier-Stokes solution was computed to determine the axial variation in static pressure along the ogive body. This pressure variation was then used as an input to a fine-grid turbulent-boundary-layer code that generated the dependent variables (U) at the upstream external flow boundary (CD). A similar boundary-

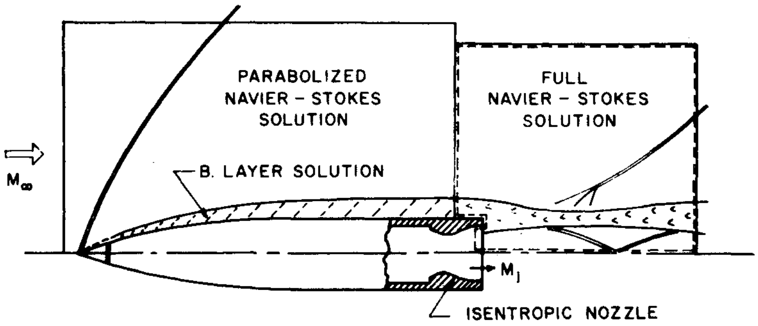

Fig. 2 Flowfield schematic for an axisymmetric nozzle in supersonic flow.

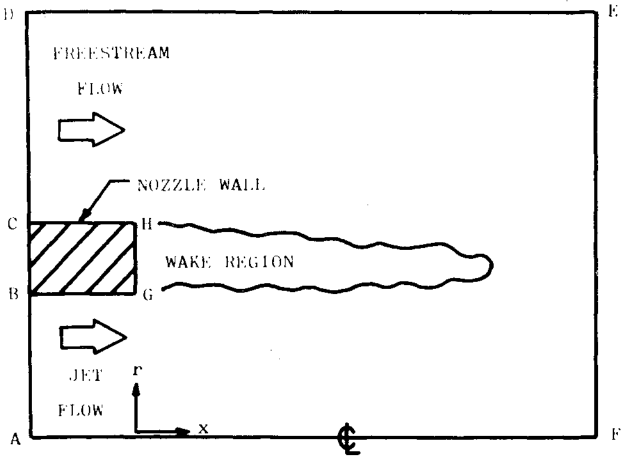

Fig. 3 Physical domain for the computational solutions.

layer solution was utilized to generate the flow profiles at the upstream jet boundary (*AB*). These boundary conditions can be expressed as:

$$U_{1,j} = U_1(r) \tag{10}$$

Outer Boundary

The outer boundary (*DE*) must accurately represent a free-flight condition where mass flow is allowed across a boundary embedded in a supersonic external flowfield. Weak shock waves and Prandtl-Meyer expansion waves must also exit this boundary without being reflected artificially back into the domain of interest. One condition that allows this is assumption of simple wave solution:[16]

$$\left.\frac{\partial U}{\partial \lambda_l}\right|_{DE} = 0 \tag{11}$$

where λ_l is the straight left-running characteristic line passing through each point on the outer boundary. This characteristic line is determined only by the value of the Mach number and flow angle of the supersonic flow present near the outer boundary.

Downstream Boundary

The downstream boundary (*EF*) is unique in that no rigorous assumptions can be made about either the variables or their gradients unless the boundary is placed a great distance downstream of the nozzle exit plane. For the case in which the downstream boundary is placed where streamwise gradients do exist, an extrapolation method is utilized. Second-order Taylor series expansions are applied at this boundary to give the following expression:

$$F_{IL,j} = 3f_{IL-1,j} - 3f_{IL-2,j} + f_{IL-3,j} \tag{12}$$

where f denotes the primitive variables ρ, u, v, and T and IL denotes the axial value of the mesh points along the downstream boundary. This extrapolation condition diverged numerically during the solution procedure for the case containing a Mach reflection with a substantial subsonic-outflow boundary region. The following first-order zero-gradient condition was therefore utilized over subsonic-outflow regions during the solution procedure to prevent this divergence problem:

$$f_{IL,j} = f_{IL-1,j} \tag{13}$$

Centerline Boundary

The centerline boundary (*AF*) is a line of symmetry with no mass or energy flux across it. The normal velocity component is then set as

$$v_{i,1} = 0 \tag{14}$$

The symmetry condition at the centerline is combined with second-order Taylor series expansions to give the following extrapolations for ρ and u:

$$\rho_{i,1} = (K^2\rho_{i,2} - \rho_{i,3})/(K^2 - 1) \tag{15}$$

$$u_{i,1} = (K^2u_{i,2} - u_{i,3})/(K^2 - 1) \tag{16}$$

where K is the ratio $r_{i,3}/r_{i,2}$. Again, for subsonic-flow regions at this boundary, the following first-order condition is applied:

$$\rho_{i,1} = \rho_{i,2} \tag{17}$$

$$u_{i,1} = u_{i,2} \tag{18}$$

Since this boundary can be considered as a streamline, a constant stagnation enthalpy condition is imposed as

$$[C_pT + (u^2/2)]\,|_{AF} = \text{const} \tag{19}$$

The required values of the conservative variables (U) can now be determined along the centerline.

Nozzle Walls

The nozzle walls are treated as no-slip, impermeable boundaries with a constant wall temperature, giving

$$u\,|_{\text{wall}} = v\,|_{\text{wall}} = 0 \tag{20}$$

$$T\,|_{\text{wall}} = T_w \tag{21}$$

The following first-order zero-pressure-gradient compatibility condition is also applied at each wall:

$$\frac{\partial P}{\partial n} = 0 \tag{22}$$

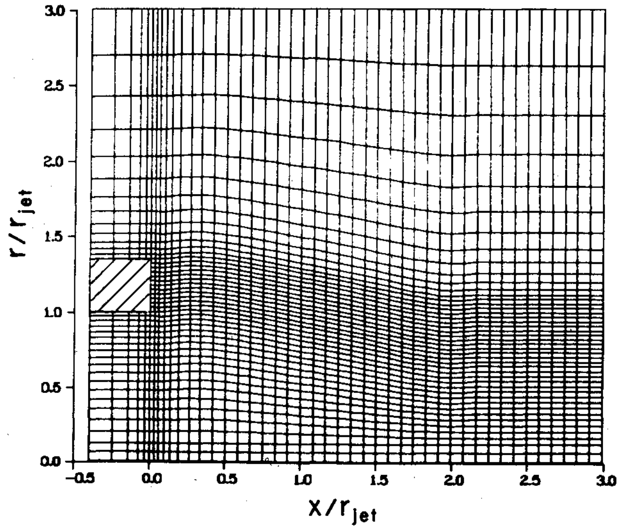

Fig. 4 Finite difference mesh, $P_j/P_\infty = 0.150$.

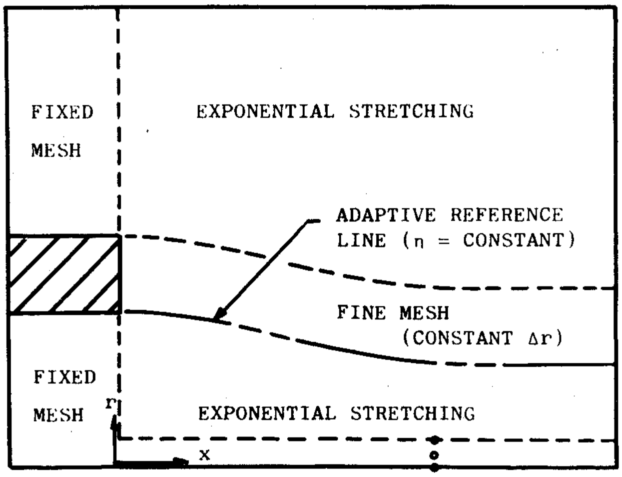

Fig. 5 Adaptive mesh schematic.

where n is in the direction normal to the wall.

Initial Conditions

Since the incoming upstream-flow variables are fixed in time, they are initially imposed over the complete computational domain as

$$U^0_{i,j} = U^0_{1,j} \tag{23}$$

The value of the u component of velocity in the nozzle wake region is also set to grow exponentially to a value close to that of the two streams in the far wake, thus accelerating convergence. Once an initial converged solution was obtained for the nozzle, each successive case was initialized by applying the new jet input profile on the jet inflow boundary of the preceding solution. This allowed a much higher convergence rate, since the flow structure in the near wake was already in existence from the previous solution.

Computational Grid System

The physical finite difference mesh for each nozzle pressure ratio case is generated numerically, with a typical example shown in Fig. 4. An exponential stretching scheme is utilized in both the axial and radial directions to keep fine mesh in viscous regions near the nozzle walls. An adaptive-mesh scheme is utilized radially in the wake of the nozzle annulus. This scheme allows the fine-mesh region of the grid to remain in the viscous mixing region as each solution progresses toward convergence. The following equation[17] is enforced along an adaptive reference line shown in Fig. 5 as the solution progresses:

$$\frac{\partial r}{\partial t} = C_a\left(v - u\frac{\partial r}{\partial x}\right) \tag{24}$$

where C_a is a constant set at 0.4 and used to damp the grid motion with respect to time. Spatial averaging of the velocity components is applied to reduce the effects of numerical velocity fluctuations at individual mesh points in the flow, and an upwind differencing finite difference form of the term $(\partial r/\partial x)$ is applied to increase stability. The adaptive reference line is set using the value of j corresponding to the nozzle inner wall for overexpanded cases and to the nozzle outer wall for the underexpanded cases. Once the position of this reference line is established at each iteration, a fine-mesh region corresponding to the nozzle wall thickness is computed. The exponential stretching scheme is then reapplied at each axial station downstream of the nozzle exit plane. This scheme is terminated once the position of the mixing layer is established for each case.

Numerical Procedure

The weak conservative form of the two-dimensional, time-dependent Navier-Stokes equations (9) is solved using MacCormack's explicit finite-difference method.[18,19] This algorithm is an efficient Lax-Wendroff-type differencing scheme of second-order accuracy that utilizes time-splitting and two-step predictor-corrector techniques. Through use of the time-splitting technique, the two-dimensional operator is separated into two one-dimensional sweep operators in the ξ and η directions. The dependent variable vector is then advanced in time as:

$$U(\xi,\eta,t+\Delta t) = [L_\xi(\Delta t/2)L_\eta(\Delta t)L_\xi(\Delta t/2)]\cdot U(\xi,\eta,t) \tag{25}$$

with $\Delta t = \Delta t_\xi$ for $\Delta t_\xi < \Delta t_\eta$, or as

$$U(\xi,\eta,t+\Delta t) = [L_\eta(\Delta t/2)L_\xi(\Delta t)L_\eta(\Delta t/2)]\cdot U(\xi,\eta,t) \tag{26}$$

with $\Delta t = \Delta t_\eta$ for $\Delta t_\eta < \Delta t_\xi$. The terms Δt_ξ and Δt_η are the maximum allowable time steps in the ξ and η directions given by the Courant-Friedrichs-Levy (CFL) limit in the following form:

$$\Delta t_\xi = \Delta S_\xi \Big/ \left[|u_\xi| + c + \frac{1}{\rho}\left\{ \frac{2\gamma}{\Delta S_\xi}\left(\frac{\mu}{Pr} + \frac{\epsilon}{Pr_t}\right) + \frac{1}{\Delta S_\eta}[-(\lambda+\lambda_t)(\mu+\epsilon)]^{1/2} \right\}\right] \tag{27}$$

and

$$\Delta t_\eta = \Delta S_\eta \Big/ \left[|u_\eta| + c + \frac{1}{\rho}\left\{ \frac{2\gamma}{\Delta S_\eta}\left(\frac{\mu}{Pr} + \frac{\epsilon}{Pr_t}\right) + \frac{1}{\Delta S_\xi}[-(\lambda+\lambda_t)(\mu+\epsilon)]^{1/2} \right\}\right] \tag{28}$$

where u_ξ, ΔS_ξ and u_η, ΔS_η are the velocities and grid cell lengths in the ξ and η directions, respectively, and c denotes the speed of sound. The actual time step used in the computations was less than this estimated maximum. Factors on the order of 0.35 were used for the nozzle solutions involving viscous wakes containing recirculation regions.

A fourth-order pressure gradient damping scheme as introduced by MacCormack and Baldwin[19] is applied to in-

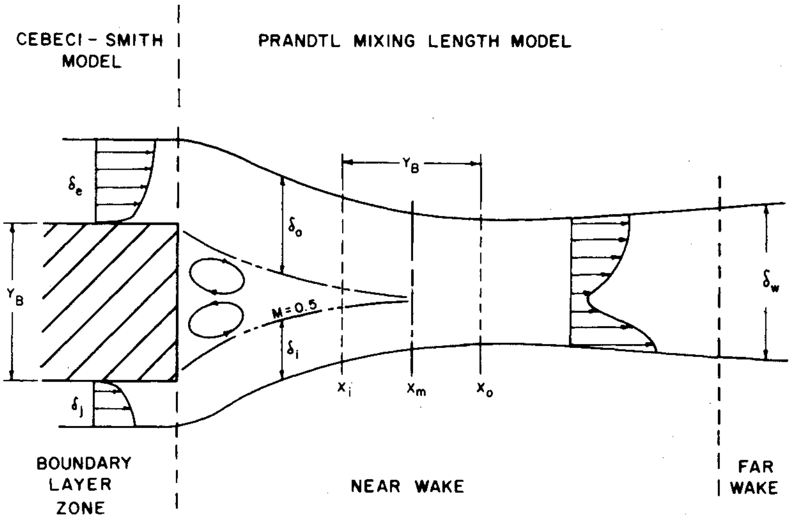

Fig. 6 Viscous-layer structure in the near wake.

crease the stability of the numerical algorithm in regions containing shock waves. This damping is applied in both the ξ and η directional sweeps, with damping coefficients set equal to 0.5 for both sweep directions.

Turbulence Modeling

Turbulence inherent to the flowfield is accounted for through application of locally dependent eddy viscosity models in the computational solutions, as shown in Fig. 6. A two-layer Cebeci-Smith eddy viscosity model[20] is utilized in the boundary-layer regions along the nozzle walls. The inner model is formulated as

$$\epsilon_i = \rho(0.4 r_n D)^2 \left| \frac{\partial u_t}{\partial r_n} \right| \tag{29}$$

where $D = 1 - \exp[-(r_n/26\mu)(\rho\tau_w)^{1/2}]$ is the Van Driest damping factor, u_t is the velocity tangential to the wall, and r_n is the distance normal to the wall. The outer model is expressed as

$$\epsilon_0 = 0.0168 \rho u_e \delta^* \gamma_k \tag{30}$$

where δ^* is the incompressible boundary-layer displacement thickness and γ_k is an intermittency factor defined as

$$\gamma_k = [1 + 5.5(r_n/\delta_{BL})^6]^{-1} \tag{31}$$

The wake region downstream of the nozzle exit plane uses another form of the Prandtl mixing length model[21] given by

$$\epsilon_w = \rho(0.065\delta)^2 \, |\omega| \tag{32}$$

where δ is the local value of the mixing-layer thickness in the radial direction and ω is the local value of vorticity. The radial vorticity profile across the mixing layer is utilized to determine the outer edges of the shear layer and thus δ at each axial position. The vorticity cutoff value was based on 10% of the maximum value in the flowfield, and gave accurate values of mixing-layer thicknesses in the wake region. In the far wake region where a single mixing layer exists, the previous definition of the length scale involving δ is valid. However, for the case of a nozzle with a thick base annulus, several length scales need to be defined in the near wake region. As shown in Fig. 6, the existence of a subsonic, recirculating "dead water" region adjacent to the nozzle base wall complicates the flow simulation. In the near wake, the length scales must make a transition from the appropriate boundary-layer thickness at the nozzle exit plane to the single-mixing-layer thickness that exists in the far wake region. The exterior edges of the mixing layers in the near wake are determined using the vorticity limit previously defined for the far wake. The interior edges of the dual shear layers are defined by the Mach 0.5 contour line surrounding the "dead water" region, as shown in Fig. 6. The wake turbulence model defined by Eq. (32) was then applied in the near wake region from the end of

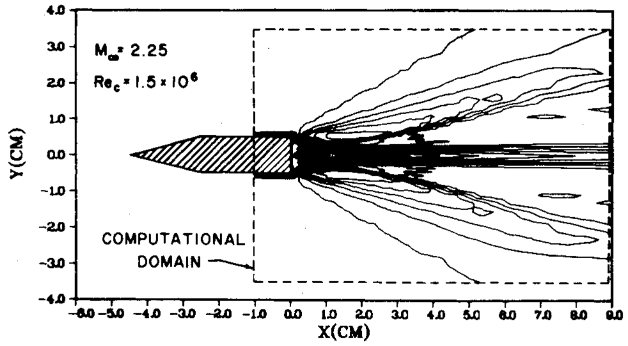

Fig. 7 Two-dimensional wedge flat plate showing computed Mach number contours.

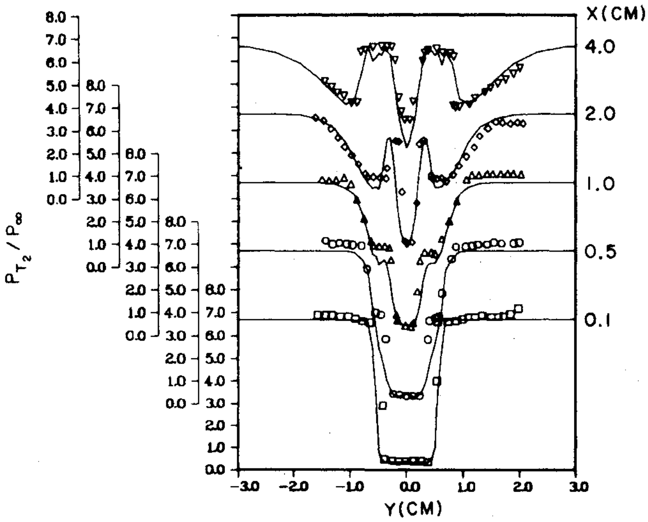

Fig. 8 Pitot pressure profiles in the near wake of the two-dimensional wedge flat plate (symbols—experimental data;[24] solid lines—computational solution).

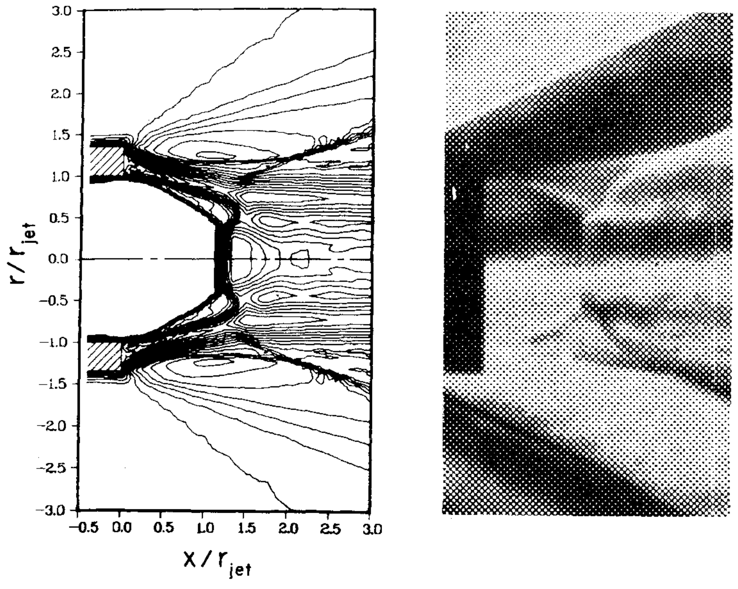

Fig. 9 Comparison between the computational nozzle solution depicted as Mach contours and the corresponding schlieren photograph, $P_j/P_\infty = 0.150$.

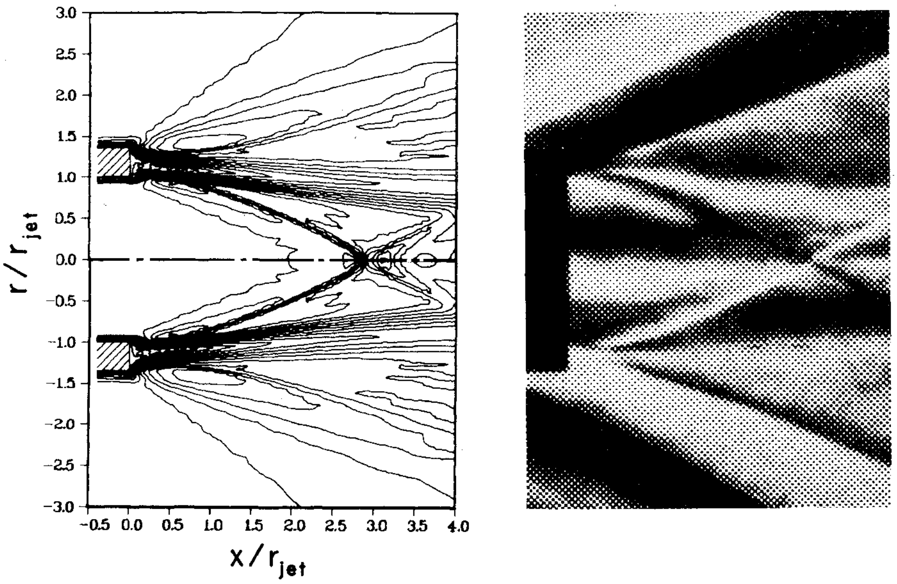

Fig. 10 Comparison between the computational nozzle solution depicted as Mach contours and the corresponding schlieren photograph, $P_j/P_\infty = 0.527$.

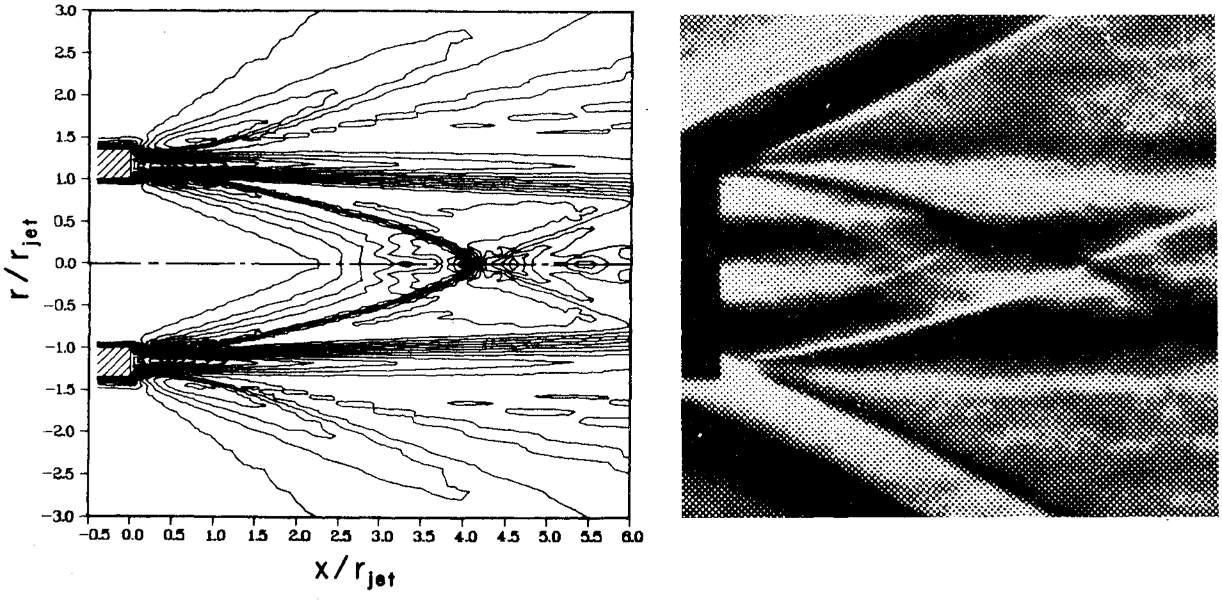

Fig. 11 Comparison between the computational nozzle solution depicted as Mach contours and the corresponding schlieren photograph, $P_j/P_\infty = 1.03$.

the boundary-layer zone to the start of the initial mixing zone, one base height in length and centered at x_m. An exponential extrapolation for δ was applied in this zone to smoothly adjust the thickness of the dual shear layers (δ_0 and δ_i) that exist in the expansion and recompression zones of the near wake region to that of the single shear layer (δ_w) in existence further downstream.

Results

Computational Details

Five numerical solutions[22] were obtained using a CDC Cyber 175 high-speed digital computer for an axisymmetric nozzle ($M_\infty = 1.94$, $M_{\text{jet}} = 3.00$, $Re_\infty = 2.2 \times 10^6$) at nozzle static pressure ratio (P_j/P_∞) conditions given experimentally.[23] Finite difference meshes consisted of 45×45 grid points for the highly overexpanded cases where the flowfield of interest is fairly compact ($P_j/P_\infty = 0.150$, 0.251), and 57×45 point grids for the other cases possessing larger axial flow domains ($P_j/P_\infty = 0.527$, 1.03, 1.59). The smallest grid spacing occurred adjacent to the nozzle walls and was set at $\Delta x/r_{\text{jet}} = \Delta r/r_{\text{jet}} = 0.030$. Each solution progressed in time until the value of the base pressure varied less than 1% during one characteristic time period defined as

$$t_{\text{ch}} = L/u_\infty \tag{33}$$

where L is the total axial length of the computational flowfield. The result was then assumed to be the asymptotic solution. Solution times ranged from approximately 2 h for cases restarted from previous solutions to 4 h for the first case started using only the boundary-layer profiles.

Comparison with Experimental Data

The thick base annulus of the experimental nozzle configuration generated a well-defined near wake region. Flow features such as a separated recirculation zone, corner flow expansions and subsequent recompressions resulting in shock waves, and the evolution of the flow in the mixing layer to a classic far wake region were evident. Experimental data in this region for the nozzle consisted only of values for the nozzle base pressure. In order to substantiate the turbulence model in the near wake region, a check case consisting of turbulent supersonic flow over a wedge flat plate was solved numerically (Fig. 7). This case[24] exhibited similar flow characteristics in the wake region and possessed more detailed experimental flow data. The numerical solution for the wedge flat plate used the previously detailed computational solver and turbulence models. The computational mesh sizing on the plate ($\Delta x_{\min}/\delta_{BL}$, $\Delta r_{\min}/\delta_{BL}$) was set identical to that of the nozzle in order to minimize differences caused by truncation error. As shown in Fig. 8, very good agreement was obtained between the experimental and computationally generated pitot pressure profiles in the near wake region. This case demonstrated that the effects of turbulence on the computed values of velocity and pressure in this region can be simulated in the nozzle solutions.

Comparisons between the numerical solutions and the experimental data for the axisymmetric nozzle can be made both qualitatively and quantitatively. Figures 9-11 give a good visual comparison between the numerical solutions depicted as Mach number contours (reflected to give a total flowfield) and the experimental schlieren photographs. All features typical of afterbody types of flow, such as the shock structure internal to the jet core flow, external recompression shocks, and shear-layer development, are readily discernible and in good agreement with the experimental data. Correct transition from regularly reflected shock waves at the line of symmetry to a strong Mach disk reflection in the jet core flow was also achieved numerically. Several other phenomena associated with afterbody flows are evident in Fig. 12, which displays computed velocity profiles at given axial stations for the large Mach disk case. The separated "dead water zone" of recirculating flow in the near wake region and development of the near wake to a far wake velocity profile are both apparent in this figure. Existence of the strong Mach disk near the centerline is very evident, with the flow in the subsonic core region behind the shock accelerating in the correct manner to a slightly supersonic condition at the outflow boundary.

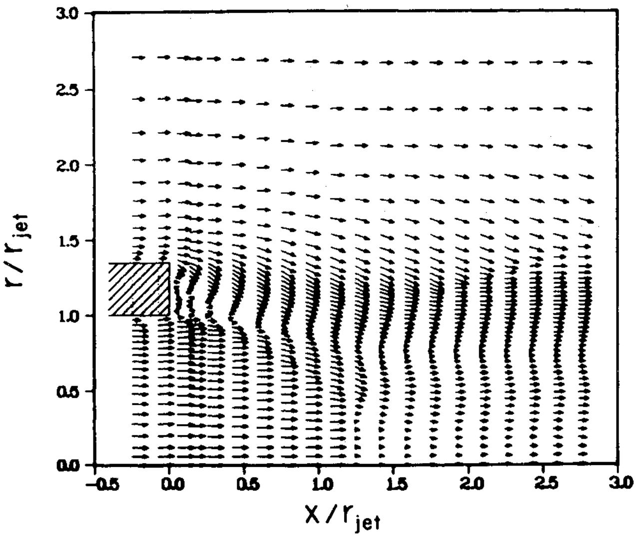

Fig. 12 Computed velocity profiles, $P_j/P_\infty = 0.150$.

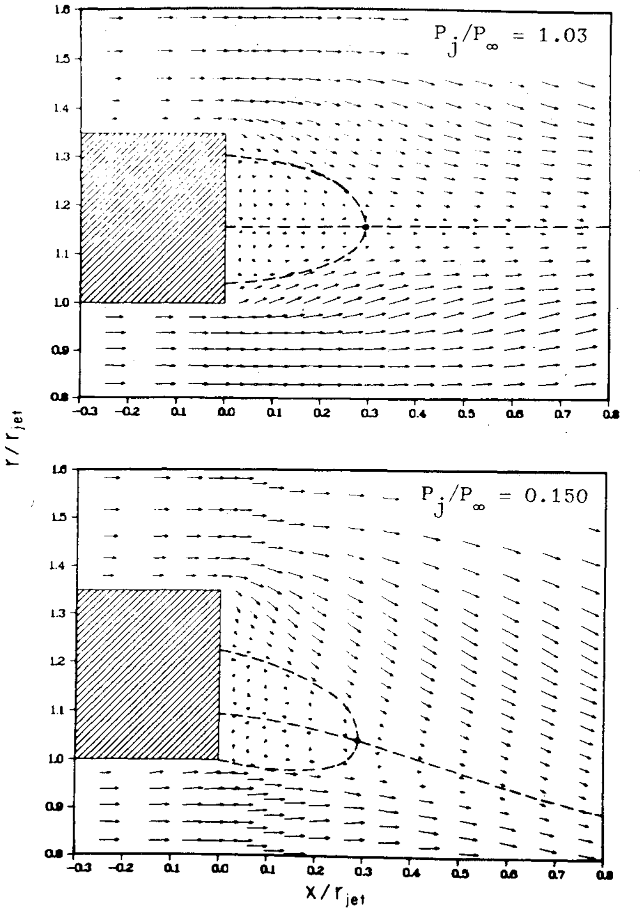

Fig. 13 Computed velocity fields in the near wake region of the nozzle base annulus.

A closer look at the near wake region is shown in Fig. 13 for two of the computational cases. This figure illustrates the change in shape of the dead water region from a

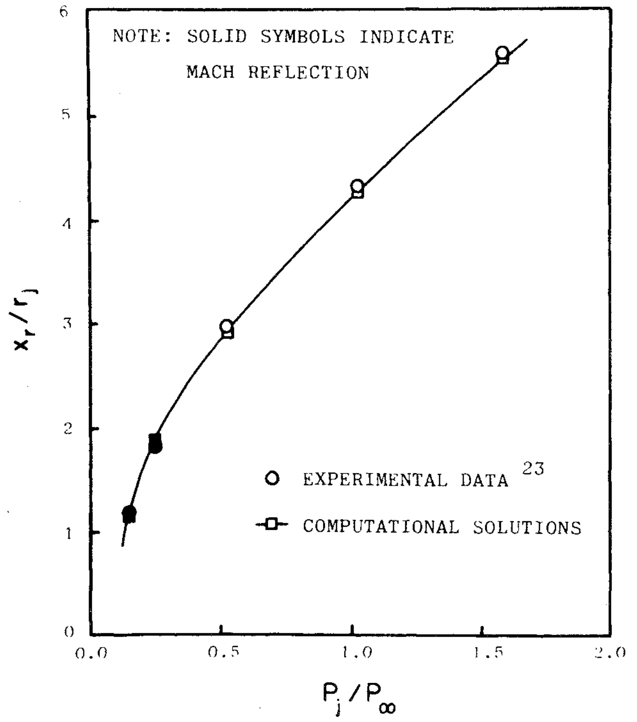

Fig. 14 Shock reflection lengths along the nozzle centerline vs nozzle static pressure ratio.

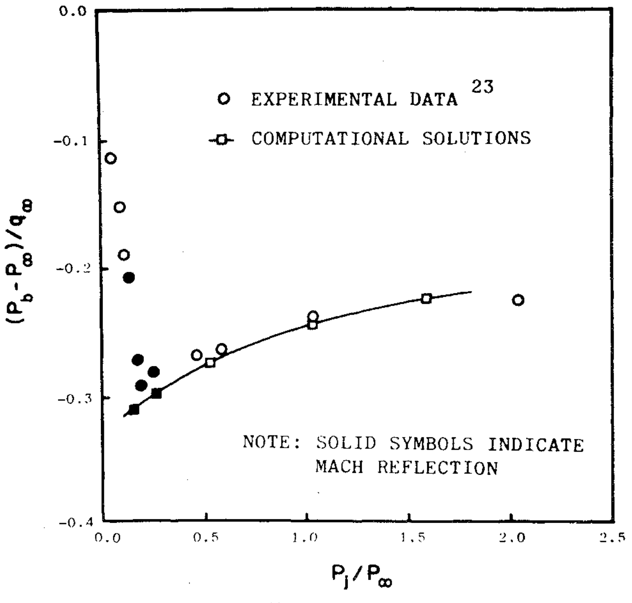

Fig. 15 Base pressure coefficient vs nozzle static pressure ratio.

predominantly symmetric nature at $P_j/P_\infty = 1.03$ to one with an asymmetric nature at $P_j/P_\infty = 0.150$. In this figure the dashed lines denote the dividing streamline and the streamlines through the stagnation point in the near wake flow for each case. Although the stagnation point in the near wake region moves radially as the jet stagnation pressure is changed, it remains in a relatively constant position axially for the cases computed.

Quantitative comparisons between the experimental data and the computed solutions are based primarily on two parameters, the axial distance along the centerline from the nozzle exit plane to the point of reflection of the incident shock wave and the value of the nozzle base pressure coefficient. This reflection length, along with the type of shock reflection, is a good indication that the inviscid flow features in the jet core caused by viscous-inviscid interactions are properly simulated. Comparisons between the experimental and computational values of these reflection lengths are shown in Fig. 14. Excellent agreement was obtained, with the computational results being within 2% of the experimental data. Values of the computed nozzle base pressure coefficient were also in good agreement with the experimental data (3-7% error), with the exception of the highly overexpanded case at which $P_j/P_\infty = 0.150$ (Fig. 15). As the pressure ratio of the nozzle is lowered, the decrease in nozzle base pressure reverses at a value of approximately $P_j/P_\infty = 0.18$ and sharply increases as the pressure ratio is further reduced. This sudden reversal in behavior is apparently due to flow separation in the divergent portion of the nozzle which prevents the jet flow from expanding fully to a Mach 3.0 state. A nonseparated condition was assumed by the experimental investigators, since the value of P_j was determined using the jet total pressure and the final area ratio of the nozzle. The computational solutions also assumed a nonseparated, Mach 3 isentropic flow just upstream of the nozzle exit plane. If separation did occur and the nozzle flow did not fully expand to a Mach 3 condition, a difference in base pressure would result. This hypothesis of separation in the nozzle was partially confirmed by computationally solving a case where the jet total pressure corresponded to the attached case ($P_j/P_\infty = 0.150$), but with the jet input profiles corresponding to isentropic expansion to a Mach number of only 2.60. A reasonable shock structure simulation was obtained, and the base pressure coefficient increased to a value of -0.265, in much better agreement with the experimental data at this condition. A more accurate simulation could be performed by extending the computational mesh back to the nozzle throat. Separation in the nozzle could then occur in a direct manner in the numerical solution.

Conclusions

Accurate solutions for an axisymmetric nozzle in a supersonic external field of flow were obtained computationally using the full Navier-Stokes equations. The numerical solutions successfully reproduced all the essential flow features, including boundary layers, corner expansions, recompression shocks, the recirculation region adjacent to the nozzle base wall, and evolution of the near wake to a flow with far wake behavior. Correct transition from regularly reflected shock waves at the line of symmetry in the jet core flow to a strong Mach disk reflection was also achieved numerically at the appropriate static pressure ratio condition of the nozzle. The subsonic embedded region immediately behind the Mach disk reflection was simulated in a correct manner.

Application of an adaptive-grid scheme in the wake region of the nozzle annulus successfully positioned the fine-mesh region of the computational grid in the wake region, which normally contains severe flow gradients. This allowed accurate simulation of this high-flow-gradient region while conserving numerical resources.

Acknowledgments

This material is based on the author's dissertation submitted in partial fulfillment of the requirements for the Doctor of Philosophy degree at the Air Force Institute of Technology, Wright-Patterson Air Force Base, Ohio.

References

[1] Grossman, B. and Melnick, R., "The Numerical Computation of the Transonic Flow over Afterbodies Including the Effect of Jet Plume and Viscous Interactions," AIAA Paper 75-62, Jan. 1975.

[2] Cosner, R. R. and Bower, W. W., "A Patched Solution of the Transonic Flowfields About an Axisymmetric Boattail," AIAA Paper 77-227, Jan. 1977.

[3] Yaeger, L. S., "Transonic Flow over Afterbodies Including the Effects of Jet-Plume and Viscous Interactions with Separation," AIAA Paper 77-228, Jan. 1977.

[4] Forester, C. K., "Numerical Simulation of the Interaction of Jet and Freestream Flows in Engine Exhaust Systems," AIAA Paper 78-144, Jan. 1978.

[5] Holst, T., "Numerical Solution of Axisymmetric Boattail Fields with Plume Simulators," AIAA Paper 77-224, Jan. 1977.

[6] Diewert, G. S., "Numerical Simulation of Three-Dimensional Boattail Afterbody Flow Field," AIAA Paper 80-1347, July 1980.

[7] Mikhail, A. G., "Numerical Solution of a Supersonic Nozzle Afterbody Flow with Jet Exhaust," AFFDL-TR-79-3078, June 1979.

[8] Peery, K. M. and Forester, C. K., "Numerical Simulation of Multi-stream Nozzle Flows," AIAA Paper 79-1549, July 1979.

[9] Abbet, M. A., "Mach Disc in Underexpanded Exhaust Plumes," *AIAA Journal,* Vol. 9, March 1971, pp. 512-514.

[10] Adamson, T. C. and Nicholls, J. A., "On the Structure of Jets from Highly Underexpanded Nozzles into Still Air," *Journal of the Aerospace Sciences,* Vol. 26, Jan. 1959, pp. 16-24.

[11] Eastman, D. W. and Radtke, L. P., "Location of the Normal Shock Wave in the Exhaust Plume of a Jet," *AIAA Journal,* Vol. 1, April 1963, pp. 918-919.

[12] Chang, I. S. and Chow, W. L., "Mach Disk from Underexpanded Axisymmetric Nozzle Flow," *AIAA Journal,* Vol. 12, Aug. 1974, pp. 1079-1082.

[13] Chow, W. L. and Chang, I. S., "Mach Reflection Associated with Overexpanded Nozzle Freejet Flows," *AIAA Journal,* Vol. 13, June 1975, pp. 762-766.

[14] Jofre, R. J., "The Mach Disc in Axisymmetric Rocket Plumes," Ph.D. dissertation, Louisiana State Univ., Baton Rouge, La., May 1971.

[15] Sinha, R., Zakkay, V., and Erdos, J., "Flowfield Analysis of Plumes of Two-Dimensional Underexpanded Jets by a Time-Dependent Method," *AIAA Journal,* Vol. 9, Dec. 1971, pp. 2362-2370.

[16] Roache, P. J., "Basic Computational Methods for Compressible Flow," *Computational Fluid Dynamics,* Hermosa Publishers, Albuquerque, N. Mex., 1972, pp. 282-283.

[17] Hirt, C. W., Nichols, B. D., and Romero, N. C., "SOLA-A Numerical Solution Algorithm for Transient Fluid Flows," Los Alamos Scientific Lab., Rept. LA-5852, April 1975.

[18] MacCormack, R. W., "An Efficient Numerical Method for Solving the Time-Dependent Compressible Navier-Stokes Equations at High Reynolds Number," NASA TM X-73.129, July 1976.

[19] MacCormack, R. W. and Baldwin, B. S., "A Numerical Method for Solving the Navier-Stokes Equations with Application to Shock-Boundary Layer Interactions," AIAA Paper 75-1, 1975.

[20] Cebeci, T., Smith, A., and Mosinskis, G., "Calculation of Compressible Adiabatic Turbulent Boundary Layers," *AIAA Journal,* Vol. 8, Nov. 1970, pp. 1974-1982.

[21] Dash, S. M., Wilmouth, R. G., and Pergament, M. S., "Overlaid Viscous/Inviscid Model for the Prediction of Nearfield Jet Entrainment," *AIAA Journal,* Vol. 17, Sept. 1979, pp. 950-958.

[22] Hasen, G. A., "Navier-Stokes Solutions for a Supersonic Coflowing Axisymmetric Nozzle with a Thick Base Annulus," Ph.D. dissertation, Air Force Institute of Technology, Wright-Patterson Air Force Base, Ohio, April 1981.

[23] Bromm, A. F. and O'Donnell, R. M., "Investigation at Supersonic Speeds of the Effect of Jet Mach Number and Divergence Angle of the Nozzle upon the Pressure of the Base Annulus of a Body of Revolution," NACA RM L54I16, Dec. 1954.

[24] Rom, J., Seginer, A., and Kronzon, J., "The Flow Field in the Turbulent Supersonic Near Wake Behind a Two-Dimensional Wedge Flat Plate Model," TAE Rept. 54, Aug. 1966.

From the AIAA Progress in Astronautics and Aeronautics Series . . .

AEROTHERMODYNAMICS
AND PLANETARY ENTRY—v. 77
HEAT TRANSFER AND THERMAL CONTROL—v. 78

Edited by A. L. Crosbie, University of Missouri-Rolla

The success of a flight into space rests on the success of the vehicle designer in maintaining a proper degree of thermal balance within the vehicle or thermal protection of the outer structure of the vehicle, as it encounters various remote and hostile environments. This thermal requirement applies to Earth-satellites, planetary spacecraft, entry vehicles, rocket nose cones, and in a very spectacular way, to the U.S. Space Shuttle, with its thermal protection system of tens of thousands of tiles fastened to its vulnerable external surfaces. Although the relevant technology might simply be called heat-transfer engineering, the advanced (and still advancing) character of the problems that have to be solved and the consequent need to resort to basic physics and basic fluid mechanics have prompted the practitioners of the field to call it thermophysics. It is the expectation of the editors and the authors of these volumes that the various sections therefore will be of interest to physicists, materials specialists, fluid dynamicists, and spacecraft engineers, as well as to heat-transfer engineers. Volume 77 is devoted to three main topics, Aerothermodynamics, Thermal Protection, and Planetary Entry. Volume 78 is devoted to Radiation Heat Transfer, Conduction Heat Transfer, Heat Pipes, and Thermal Control. In a broad sense, the former volume deals with the external situation between the spacecraft and its environment, whereas the latter volume deals mainly with the thermal processes occurring within the spacecraft that affect its temperature distribution. Both volumes bring forth new information and new theoretical treatments not previously published in book or journal literature.

Volume 77—444 pp., 6×9, illus., $30.00 Mem., $45.00 List
Volume 78—538 pp., 6×9, illus., $30.00 Mem., $45.00 List

TO ORDER WRITE: Publications Dept., AIAA, 1290 Avenue of the Americas, New York, N.Y. 10104